Draft version August 30, 2016
Preprint typeset using LaTeX style AASTeX6 v. 1.0

CONSTRAINING HABITABILITY AND ATMOSPHERIC PROPERTIES THROUGH REFLECTED LIGHT OBSERVATIONS OF TERRESTRIAL EXOPLANETS

Y. Katherina Feng[1,2], Tyler D. Robinson[1,3]

[1]Department of Astronomy & Astrophysics, 1156 High Street, University of California, Santa Cruz, CA 95064, USA.

[2]NSF Graduate Research Fellow

[3]Sagan Postdoctoral Fellow

ABSTRACT

We present the first systematic exploration of atmospheric retrievals on simulated reflected-light data for terrestrial exoplanets. Our initial forward model can constrain three key characteristics relevant to habitability: water vapor mixing ratio, surface pressure, and ozone mixing ratio. To examine the feasibility of constraining these quantities with a future high-contrast instrument (e.g., a starshade paired to NASA's WFIRST mission), we simulate data over a range of spectral resolutions ($R = \lambda/\Delta\lambda$ = 35, 70, and 140) and qualities (signal-to-noise of 5, 10, and 20). Our noise simulations are non-gray, and rely on a published high-contrast imaging and spectroscopy instrument model. This investigation highlights a consistent and accurate ozone detection for an Earth-twin across nearly all observational configurations. However, for water vapor mixing ratio and surface pressure retrievals, we find that cloud parameterizations and assumptions are critical to making accurate inferences. We discuss future work and improvements, including extensions to super-Earths and mini-Neptunes.

1. INTRODUCTION

The scientific field of exoplanets has been rapidly advancing since the hallmark discovery of the first planet orbiting a Sun-like star other than our own (Mayor & Queloz 1995). Following the launch of NASA's *Kepler* mission (Borucki et al. 2003, 2011), the field has seen the discovery of thousands of transiting exoplanets and the exciting result that planets with radii between 0.75–2.5 $R_\oplus$ are common around solar-type stars (Burke et al. 2015). Only within the last decade have observational studies of exoplanet atmospheres seen substantial development, starting with the first detection of an exoplanet atmosphere by Charbonneau et al. (2002). However, nearly all atmospheric characterization studies have focused on hot Jupiters—owing to their large sizes and high temperatures—instead of the terrestrial-sized planets that make up the bulk of *Kepler*'s yield.

Recently, de Wit et al. (2016) have studied the combined transmission spectra of two transiting Earth-sized planets orbiting the ultracool dwarf TRAPPIST-1. While no gas absorption features were detected by de Wit et al. (2016), this work highlights the improvements in signal size when terrestrial-sized transiting planets are studied around low-mass stars. Additionally, since the Habitable Zones around low-mass stars are relatively close-in, characterization studies of potentially habitable exoplanets around cool stars can benefit from the frequency of transit events. Unfortunately for Sun-like stars, the Habitable Zone is located far from the star, making transit events rare and infrequent, thus limiting the potential for atmospheric characterization. For these worlds, direct imaging is emerging as a valuable technique for studying the atmospheres of planets at larger separations from their host star. Thus far, high contrast imaging has been proven successful at studying atmospheres of young, self-luminous exoplanets in the near-infrared (e.g., Barman et al. 2011; Macintosh et al. 2015). But, in the near future, NASA's Wide-Field InfraRed Survey Telescope (WFIRST, Spergel et al. 2013) will extend direct imaging studies to reflected light observations of cool gas giant exoplanets, and may even push into the regime of sub-Neptune and terrestrial exoplanets (Robinson et al. 2016).

The WFIRST mission was identified as the top priority space mission in the 2010 National Academy of Sciences decadal survey of astronomy and astrophysics.[1] With its 2.4 m primary mirror and envisioned coronagraphs, WFIRST will study the atmospheres of relatively cool planets that have been previously detected by the radial velocity technique, and will also survey stars in the solar neighborhood for planetary companions (Burrows 2014; Greco & Burrows 2015;

[1] http://sites.nationalacademies.org/bpa/bpa_049810

Spergel et al. 2015). Reflected light in the visible probes to atmospheric depths of up to $\sim$ 10 bar for giant planets (Marley et al. 2014), which is complimentary to the low pressures probed in transit observations. The wavelength range of 0.4 μm to 1.0 μmholds rich information about a planet's atmosphere. We can expect methane and water vapor absorption as well as haze absorption and cloud reflectance (Burrows 2014).

One anticipated feature/issue of the WFIRST coronagraphs will be their low optical throughput for the planetary signal, which is expected to be $\sim 1\%$ (Traub et al. 2016) and stems primarily from the complexities of accommodating for WFIRST's on-axis secondary mirror and support structures within the high contrast instruments. When noise is dominated by the detector performance, the integration time required to achieve a given signal-to-noise ratio scales as the square of the throughput times the planet flux. Thus, while the WFIRST coronagraphs provide raw contrast levels appropriate for detecting terrestrial-sized exoplanets, the small size of these planets and the low instrument throughputs make characterization impossible. If, however, we pair WFIRST with an external starshade to suppress a host star's light, we can increase throughput by at least an order of magnitude (Turnbull et al. 2012), thereby opening up the possibility of characterizing sub-Neptune and terrestrial-sized exoplanets with WFIRST. To date, though, there does not exist any systematic studies of atmospheric characterization of small exoplanets using retrieval techniques on reflected light observations.

Marley et al. (2014) considered the spectra we can expect from known radial velocity gas giants as observed with a space-based coronagraph. Given the diversity of cool giant planets, the model spectra have a variety of such input assumptions as clouds, surface gravity, and atmospheric metallicity. Marley et al. (2014) also applied the retrieval method, powered by Markov Chain Monte Carlo (MCMC), to these synthetic spectra, enabling the exploration of how well atmospheric parameters are constrained under varying quality of data. Lupu et al. (2016) further investigated the feasibility of characterizing cool giant planet atmospheres through retrieval, focusing on the ability to constrain CH_4 abundance and cloud properties. The systematic study of the impact of conditions like signal-to-noise ratios or wavelength resolution is essential to quantifying the scientific return of these reflected light observations.

This work presents our extension of these techniques into the terrestrial regime. We construct a forward model with Rayleigh scattering due to N_2 and absorption from H_2O and O_3, characteristic features of the Earth's atmosphere in the visible wavelength range of 0.4 μm to 1.0 μm (see Figure 1). We retrieve for these quantities from data sets of varying wavelength resolutions and signal-to-noise ratios. A retrieval framework such as this allows us to quantify the uncertainties associated with the parameters and search for optimal observing conditions to achieve the scientific goal of identifying traits associated with habitability.

Our report is structured as follows: Section 2 explains our forward model, how we generate simulated data, and retrieval setup. Section 3 presents the retrieval results from nine sets of simulated data. We discuss our findings in Section 4 and conclude with future work.

2. METHODS

The three essential components of our framework are simulated "observations", a forward model, and a means of evaluating the goodness of fit and corresponding acceptable range for parameters in our forward model. Our study builds upon previous work by Lupu et al. (2016), which examined systematically the interpretation of simulated direct imaging data from gas giants through Bayesian inference. In their retrievals, Lupu et al. (2016) considered the performance of both `emcee` (Goodman & Weare 2010; Foreman-Mackey et al. 2013), a Markov Chain Monte Carlo (MCMC) ensemble sampler, and `MultiNest` (Feroz & Hobson 2008; Feroz et al. 2009), a multimodal nested sampling algorithm. These two methods were shown to produce consistent results, and we select `emcee` to sample parameter posteriors in this initial investigation.

To generate model data, we modify the forward model presented in Lupu et al. (2016), which we tailor to terrestrial atmospheres by including a reflective surface, Rayleigh scattering by N_2, and absorption due to H_2O and O_3. We evaluate the model data using `emcee` against simulated observed data created by combining spectra from a 3D model of Earth (Robinson et al. 2011) with an instrument noise model appropriate for space-based direct imaging (Robinson et al. 2016).

2.1. *Forward Model*

The observed quantity for reflected light from an exoplanet at a given phase (i.e., planet-star-observer) angle α is the wavelength-dependent planet-to-star flux ratio,

$$\frac{F_p}{F_s} = A_g \Phi(\alpha) \Big(\frac{R_p}{r}\Big)^2, \tag{1}$$

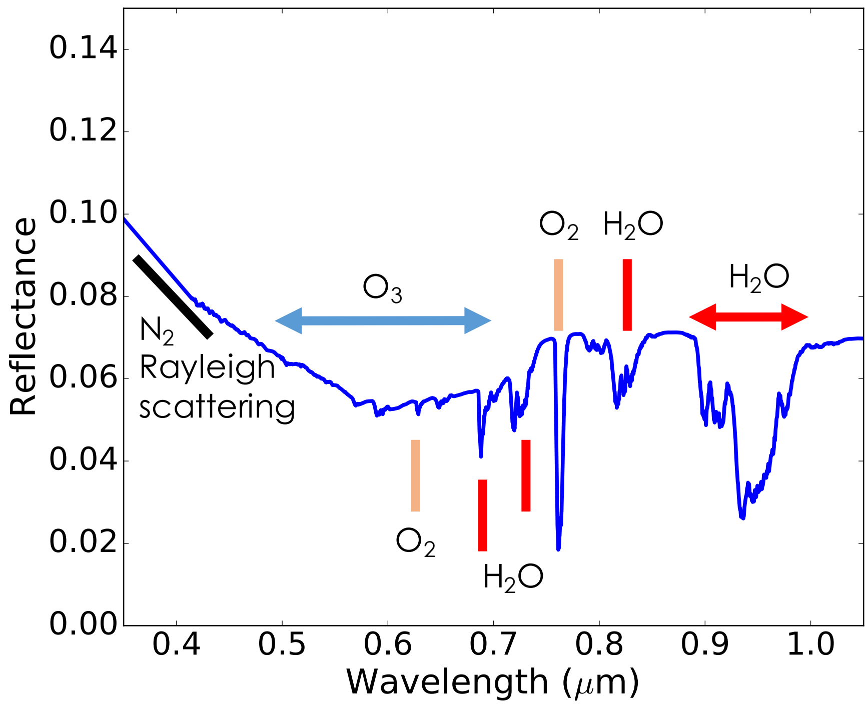

Figure 1. Spectrum of Earth at quadrature spanning wavelengths between 0.35 μm and 1.05 μm. Prominent features include the Rayleigh slope due to air molecules ($N_2$and O_2), the broad O_3 Chappuis band between 0.5 and 0.7 μm, O_2 absorption at 0.76 μm and 0.63 μm. Other features are attributed to H_2O, especially at 0.94 μm.

where A_g is the geometric albedo, $\Phi(\alpha)$ is the phase function, R_p is the radius of the planet, and r is the orbital separation. The phase function describes brightness at different phase angles and it is normalized to unity at full phase, $\alpha = 0°$. The geometric albedo is the ratio between the measured light from the planet at full phase to that from a perfectly reflecting Lambert disk with the size of the planet. Note that a Lambert surface scatters isotropically. We denote the product of the geometric albedo and the phase function as the phase-dependent "reflectance" of the planet. In general, the geometric albedo encodes the pressure-dependent composition (or "state") of an atmosphere, while the phase function represents the scattering properties of the atmosphere (Burrows 2014).

We adopt a well-known albedo code to model the reflected light spectrum of an Earth-sized planet. Our albedo code has been applied to a large variety of planetary bodies over the last two decades (see McKay et al. 1989; Marley et al. 1999; Cahoy et al. 2010), thereby demonstrating the flexibility of this model. Most recently, Lupu et al. (2016) modified the code to include parameterized 1- and 2-layer cloud models.

In our albedo code, the illuminated hemisphere of the planet is divided into latitude/longitude patches, which we sample at a resolution of 100 grid points. The wavelength-dependent brightness of each patch is determined using a plane-parallel radiative transfer solver (Toon et al. 1989). The solver incorporates two angles, both defined with respect to the local normal: θ_0, the incident angle for the stellar irradiance; and θ_1, the observed scattering angle, directed towards Earth (or the observer). Every plane-parallel patch has an atmospheric column of 60 layers.

The geometric albedo code computes a spectrum by integrating over the outgoing intensities from each facet of the surface. The integration is through Chebyshev-Gauss under two-dimensional planetary coordinates as outlined by Horak (1950) and Horak & Little (1965). The radiative transfer is calculated individually for each column of atmosphere. The source function involved is approximated by the two-stream solution to a diffuse, angle-independent radiation field (Toon et al. 1989). As described in Cahoy et al. (2010), two-stream quadrature is used to determine the upward and downward diffuse fluxes, producing the column intensity for the integration that produces the albedo spectrum.

For simplicity, we maintain the atmosphere as isothermal with a temperature of 250 K, as temperature has little effect on the reflected-light spectrum of each patch. It is important to note that we assume a cloud-free atmosphere for this investigation. The chemical abundances in our forward model atmosphere are constant as a function of pressure, and we adopt a uniform acceleration due to gravity of 9.8 m s^{-2}. At the base of the atmosphere, we establish a reflective surface by assigning a Bond albedo of $\omega = 0.3$. The Bond albedo represents the power in scattered, outgoing radiation compared to the amount of incident radiation. For the inhomogeneous surface of Earth, featuring oceans and continents, the bond albedo is wavelength-dependent, but an approximate average is 0.3 (e.g., Pallé et al. 2004). This value also encompasses the cloudy and clear scenes on Earth – it is higher than that of a completely clear atmosphere and acts as a way to offset our cloud-free assumption.

Before the addition of atmospheric features, we undertook a test to check that our reflective lower boundary condition was implemented correctly. Without atmospheric absorption or scattering, our assumption of a Lambertian surface would imply that our albedo code should follow the analytic Lambertian phase function:

$$\Phi_{\mathrm{L}}(\alpha) = \frac{\sin\alpha + (\pi - \alpha)\cos\alpha}{\pi}. \tag{2}$$

For a Lambert sphere the geometric albedo relates to the Bond albedo as $A_g = \frac{2}{3}\omega$. We have defined $\omega = 0.3$ and calculate the reflectance for different phase angles and normalize by the value at $\alpha = 0°$ to construct the model phase function. Figure 2 compares the model phase function with the analytic phase function and shows complete agreement, confirming that our treatment of the surface is correct.

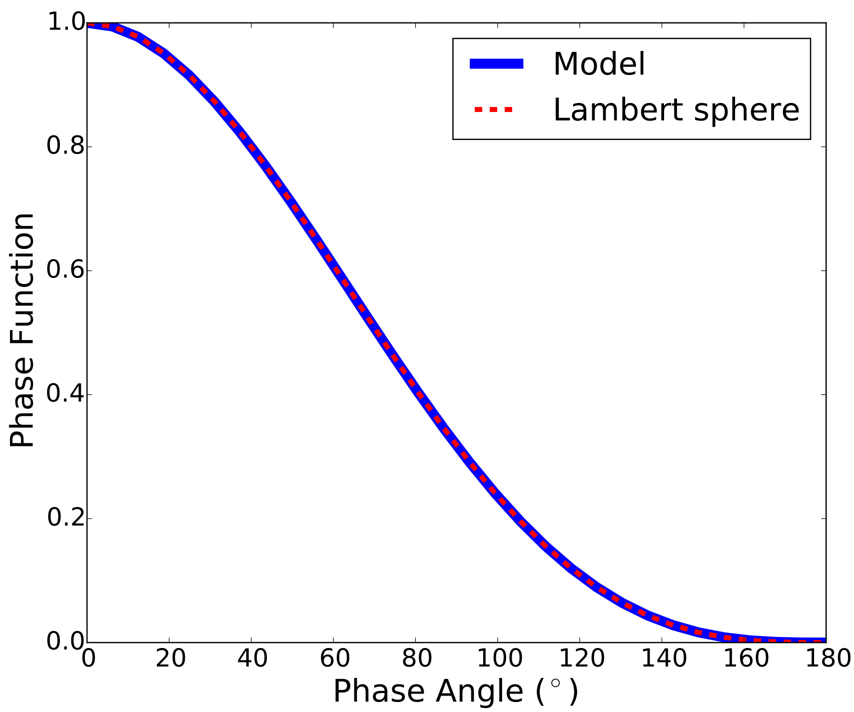

Figure 2. Comparing our model phase function to the analytic Lambertian phase function (Equation 2). No atmospheric absorption or scattering are present in the forward model. We set the surface Bond albedo to 0.3, and normalize by the reflectance at phase angle $\alpha = 0°$.

To further build an Earth-like atmosphere, we update our albedo code to include $H_2O$and O_3, which are dominant absorbers, and N_2, which is the primary Rayleigh scatterer. The absorption opacities are generated line-by-line from the HITRAN2012 line list, and span 0.3 μm to 1.0 μm. The Rayleigh scattering is treated according to Hansen & Travis (1974) with constants to describe the scattering properties of N_2 from Cox (2000).

2.2. *Simulated Data*

Our simulated observations are of an Earth-twin orbiting a Sun-like star. High spectral resolution simulated data come from a sophisticated three-dimensional (3D) model known as the NASA Astrobiology Institute's Virtual Planetary Laboratory 3D line-by-line, multiple scattering spectral Earth model (Robinson et al. 2011). The Robinson et al. (2011)

tool can simulate images and disk-integrated spectra of Earth from the ultraviolet to the infrared. It has been validated against observed data taken by NASA's EPOXI mission, which included disk-integrated near-infrared spectra and visible wavelength photometry. Because our observations of exoplanets only yield disk-integrated spectra, it is advantageous to have an accurate model that allows for arbitrary viewing geometry and phases.

Atmospheric features of the Robinson et al. (2011) model include Rayleigh scattering due to air molecules, realistic patchy clouds, and gas absorption from a variety of molecules, including H_2O, CO_2, CH_4. Surface coverage of different land types (e.g., forest, desert) is informed by satellite data, and water surfaces incorporate specular reflectance of the Sun. A grid of thousands of surface pixels are nested beneath a grid of 48 atmospheric pixels, all of equal area. For each surface pixel, properties from the overlying atmospheric pixels are used as inputs to a full-physics, plane-parallel radiative transfer solver— the Spectral Mapping Atmospheric Radiative Transfer (SMART) model (Meadows & Crisp 1996). Intensities from this solver are integrated over the pixels with respect to solid angle, thereby returning a disk-integrated spectrum.

We simulate noise in our observations using an instrument model developed by Robinson et al. (2016) for space-based direct imaging missions. For simplicity, we only include read noise and dark current, as (Robinson et al. 2016) showed that detector noise will be the dominant noise source in WFIRST spectral observations of exoplanets. Here, then, the signal-to-noise ratio is simply,

$$\mathrm{SNR} = \frac{c_p \times t_{\mathrm{int}}}{\sqrt{(c_d + c_r) \times t_{\mathrm{int}}}}, \tag{3}$$

where t_{int} is the integration time, c_p is planet count rate, and c_d is the dark noise count rate, and c_r is the read noise count rate. More rigorously, it can be shown that SNR $\propto qA_g\Phi(\alpha)B_\lambda$, where q is the wavelength-dependent detector quantum efficiency and B_λ is the stellar Planck function. Thus, when scaled to a given signal-to-noise ratio at a certain wavelength, the calculation of the signal-to-noise ratio at other wavelengths is independent of the imaging raw contrast or throughput of the instrument. As mentioned earlier, though, the integration time required to achieve a given signal-to-noise ratio is proportional to instrument throughput squared, implying that the types of observations discussed here may only be achievable if WFIRST were paired to a starshade. For our study, we will consider multiple wavelength resolutions, R, and signal-to-noise ratios. Because the signal-to-noise ratio is dependent on wavelength, we reference our values to be at 550 nm for all resolutions.

2.3. *Retrieval*

A retrieval operates by first taking a set of input parameters to calculate a noise-free, high resolution spectrum via the forward model. This spectrum is then convolved with an instrument model to the resolution of the (simulated) observations for comparison. We evaluate the fit by determining the likelihood, which describes the probability of the observed noisy data given the forward model and the set of input parameters. This procedure is repeated many times in order to adequately sample the posterior distributions of the model parameters. A standard method of doing so is via a Markov chain Monte Carlo, which we implement using `emcee`.

With each iteration of the posterior sampling, we use a different set of input parameters drawn from their respective prior distributions. The input parameters for our retrieval model are the H_2O abundance, the O_3 abundance, and a surface pressure scale factor, P_0. The scale factor is a multiplicative factor applied to a normalized 60-layer pressure grid that is 1 bar at the surface. Surface pressure is a proxy for the amount of N_2 present because this is the sole Rayleigh scatterer in our forward model. The higher the surface pressure is, the more N_2 there is to produce scattering, thus changing the extent of the slope seen in Figure 1. All three prior distributions are flat. For the H_2Oabundance, the prior extends from a volume mixing ratio of 10^{-8} to 10^{-1}. For O_3, the prior covers 10^{-10} through 10^{-1}. The upper limit is set such that these molecules do not contribute to Rayleigh scattering. The N_2 abundance is calculated by subtracting the abundances of H_2O and O_3 from 1. The prior distribution for P_0 has a range of 10^{-3} to 100.

2.3.1. *Validating the retrieval*

We validate our retrieval process by generating three sets of data with our forward model (i.e., not the 3D spectral Earth model) for an Earth-like planet seen at full phase ($\alpha = 0°$) and adding noise using the instrument model as described above. The input values we chose to generate the data are $H_2O = 3 \times 10^{-3}$, $O_3 = 7 \times 10^{-7}$, and $P_0 = 1$ such that the surface pressure is 1 bar. These abundance values are characteristic of a standard Earth model atmosphere with vertically- and spatially-varying water vapor mixing ratios (McClatchey et al. 1972). Our three data sets have resolutions of $R = 35$, 70, and 140 respectively, all with SNR $= 20$. Figures 3 illustrates the posterior distributions for $R = 70$. In all three cases, we accurately recover the input values, with an increase in precision as resolution increases.

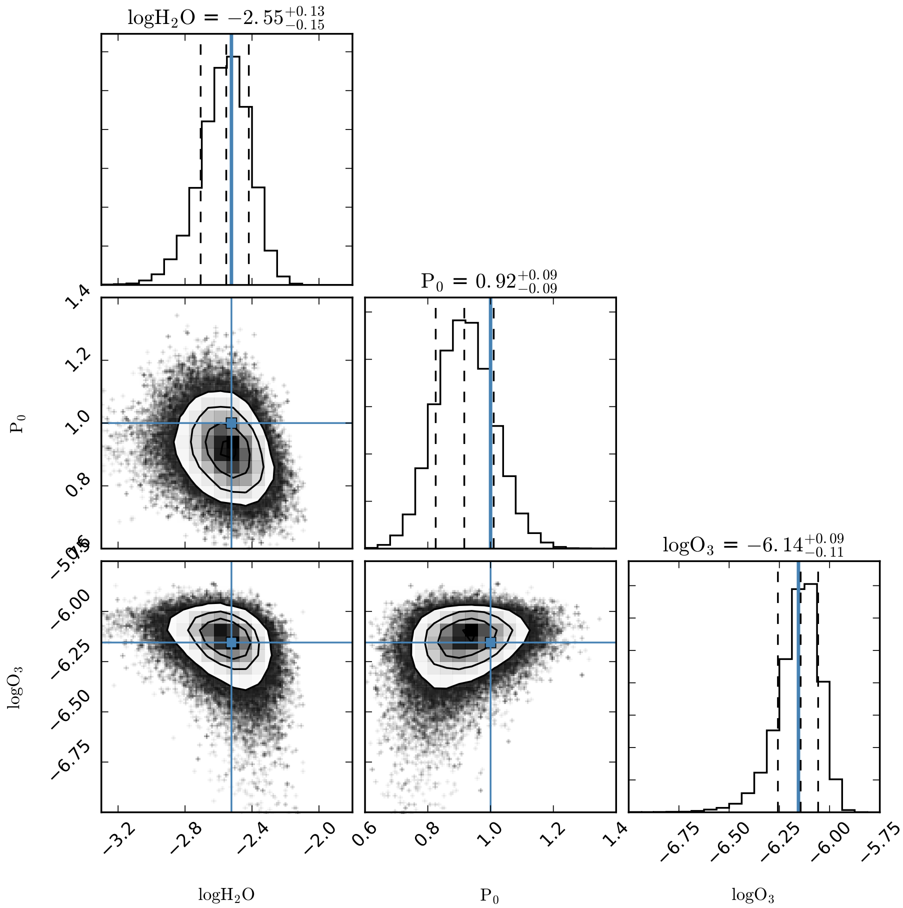

Figure 3. For simulated data using the forward model (R = 70, SNR = 20). Posterior distributions and correlations for H_2O, O_3, and P_0. The blue solid lines indicate the true input values.

3. RESULTS

Using the method described in Section 2.2, we create nine sets of data to retrieve upon, all covering 0.4 μm to 1 μm for an Earth-like planet seen at the quadrature phase ($\alpha = 90°$) around a Sun-like star. We consider three resolutions, R = 35, 70, 140; for each resolution, we consider three signal-to-noise ratios, SNR = 5, 10, 20. The range of resolutions and signal-to-noise ratios allows an exploration of the data conditions under which we can infer robust quantities.

In order to determine if the retrievals return robust estimates, we need to establish appropriate "input" or comparison values from a realistic state of Earth's complex atmosphere. Because our final simulated data are not generated from our forward model but instead a 3D model, there is no definitive single "true" value for each of our inputs. A more realistic comparison would be against a range for the mixing ratios. We consider mixing ratios from the InterComparison of Radiation Codes in Climate Models (ICRCCM, Ellingson & Fouquart 1991) for the mid-latitude summer atmosphere, which is an approximation for the average state of Earth. We construct "contribution functions" or Jacobians for H_2O and O_3 based on perturbations to the SMART model's radiative transfer. Each perturbation to a mixing ratio results in changes in the optical depth and outgoing reflected flux. Figure 4 shows the changes in reflectance with respect to changes in mixing ratios as a function of pressure and wavelength. For H_2O, the molecular abundances over the range where the contribution functions peak is 3×10^{-3} to 2×10^{-2}, with the dominant contribution at 1×10^{-2}. Similarly, for O_3, we should expect to detect a range of 2×10^{-6} to 8×10^{-6}, with the dominant contribution at 4×10^{-6}.

In Figure 5, we see the resulting spectral fits to the data after the retrievals, highlighting the cases of SNR $= 5, 10, 20$ for $R = 35, 70, 140$ respectively. As seen in Figure 1, H_2O has a prominent absorption feature at 0.94 μm. In the low and medium resolution cases ($R = 35, 70$), there is a large spread in fits to this feature, suggesting H_2O is not well-constrained. Figure 6 shows the posterior distributions for all nine retrievals for water vapor mixing ratio. Except

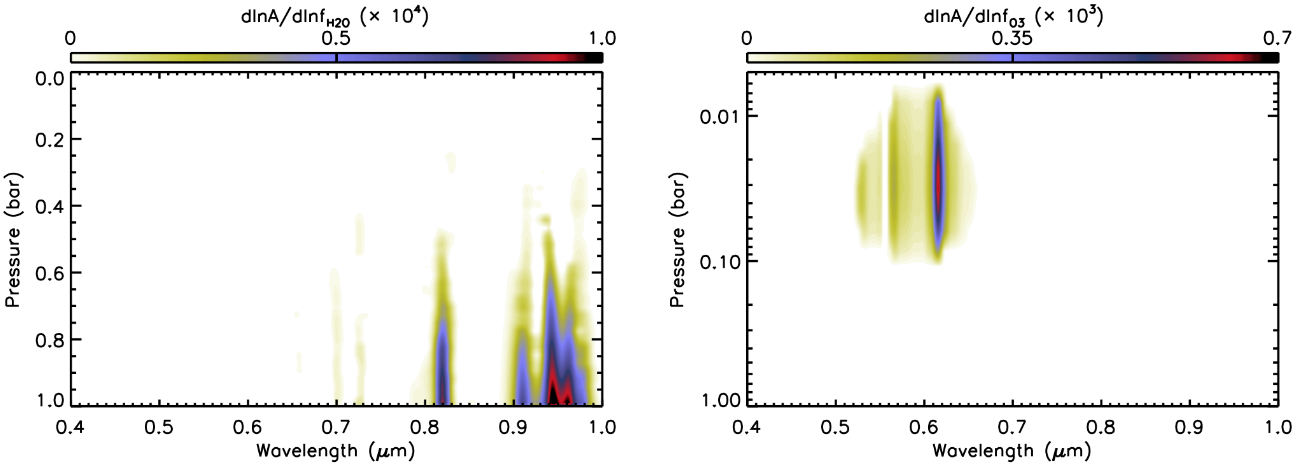

Figure 4. *Left:* The change in reflectance due to changes in mixing ratio of H_2O. *Right:* The change in reflectance due to changes in mixing ratio of O_3. These show where in the atmosphere (pressure-wise) and wavelength space that changes in the mixing ratio of each molecule lead to fractional changes in reflectance.

for the upper limit in the case of $R = 35$, SNR $= 5$, there is detection of water vapor, with increasing confidence as the resolution and signal-to-noise ratio improve. When compared to the expected range as determined above, there is a bias to mixing ratios $0.5 - 1.0$ order of magnitude lower.

Figure 7 presents the posterior distributions for all nine cases for the surface pressure. All distributions overlap, and there is detection across all resolution and SNR combinations. However, once again there is a bias for the retrieved quantity to be lower than the expected value—the retrievals commonly return a value near 0.3 bar instead 1 bar, which is the true value for Earth.

Our third and final retrieved parameter is O_3 mixing ratio. Unlike the previous two, the posterior distributions fall within the expected range as seen in Figure 8. As resolution and signal-to-nosie ratio improve, there is accurate convergence to the peak value of 4×10^{-6} determined from the Jacobian.

Figures 6 through 8 all include a summary panel for the relevant retrieved parameter that only displays the posteriors distributions for the case of SNR $= 10$ at the three resolutions. The highest SNR of 20 may be unrealistic to obtain, so it is encouraging that at the medium SNR of 10, we have constrained posterior distributions for all parameters. Even in the case of SNR $= 5$, there is only one instance of an upper limit. However, we note that the comparatively low values obtained for H_2O and surface pressure likely indicate that our forward model may be overly simplified. Based on the summary panels, we see that minimal improvements are made by going to the high resolution of $R = 140$, especially in the case of O_3 for which there are accurate posterior distributions at all lower resolutions. This suggests that a high resolution instrument is not necessary to be able to detect these quantities of interest.

4. DISCUSSION

Our retrieval results show bias toward lower values for both water vapor mixing ratio and surface pressure. This is likely the result of our cloud-free atmosphere assumption. Recall that the simulated observations are produced by a 3D model which includes realistic patchy clouds. These clouds can act to "truncate" the atmospheric column over more than half of the observed disk. As a result, we effectively see a decreased water vapor column abundance, as compared to a clear-sky only model. Furthermore, the water vapor contribution functions in Figure 4 indicate that our abundance estimates would be strongly affected by clouds, which usually occur between pressures of 0.3 and 0.8 bar.

Because surface pressure is indicative of the amount of N_2 that can do Rayleigh scattering, decreased Rayleigh scattering optical depth implies a lower retrieved surface pressure. As was the case with water vapor, the presence of clouds can cut short the depth to which we can see into the atmosphere. A scattering optical depth of unity is reached in the clouds before we reach an optical depth of unity for Rayleigh scattering. In other words, the Rayleigh slope in the observations is a superposition of the weak Rayleigh slope that occurs for cloudy scenes and the strong Rayleigh slope that occurs for clear-sky scenes. Thus, when fit with a cloud-free forward model, the average surface pressure we retrieve will be less than 1 bar, and is typically ~ 0.3 bar.

Clouds did not bias our retrieval of O_3 because, as Figure 4 shows, O_3's contribution functions peak above where clouds lie in the atmosphere. The accurate retrieval of O_3 is an exciting finding, since O_3 is a biosignature gas that

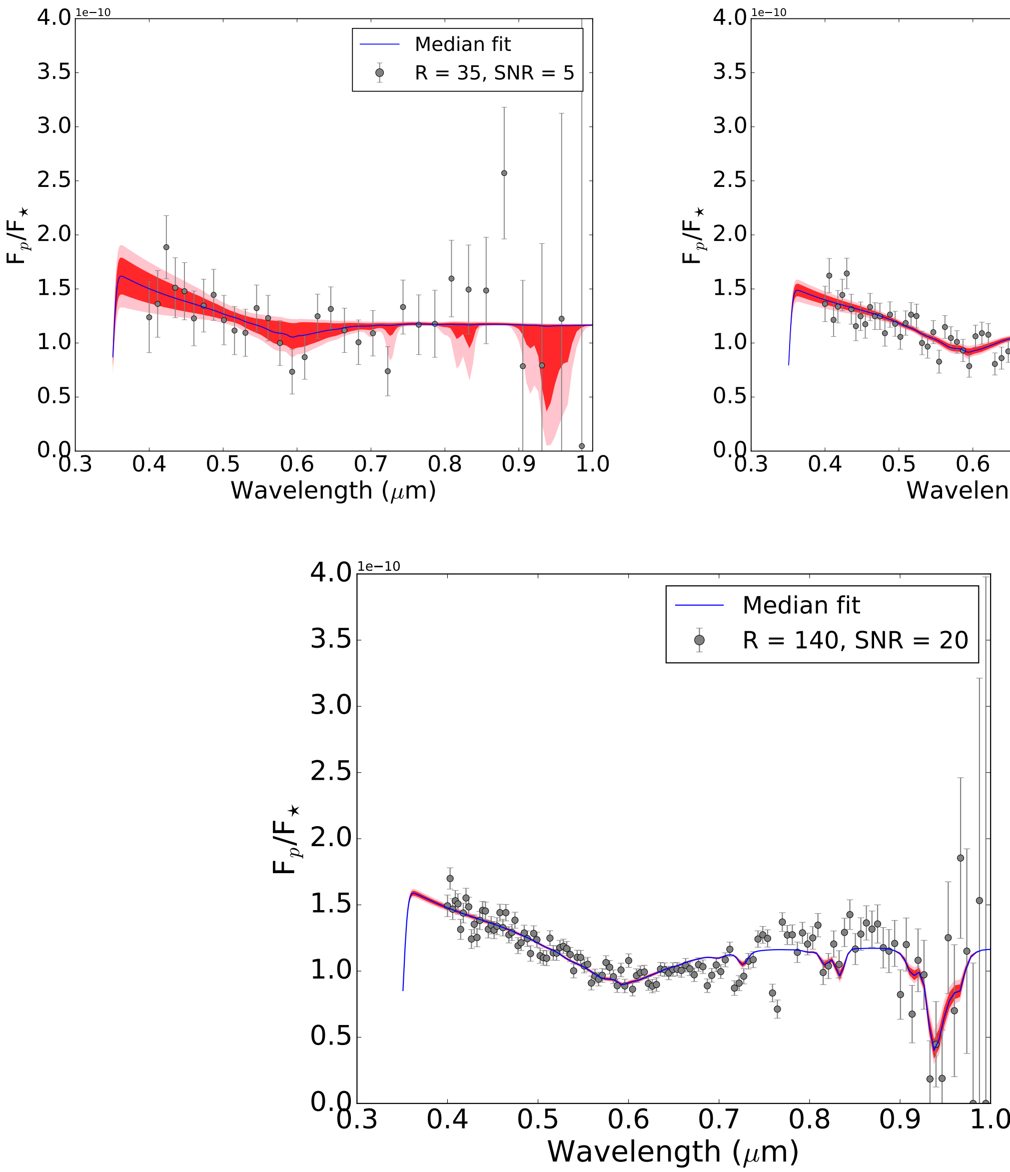

Figure 5. Simulated data for $R = 35, 70, 140$ at SNR $= 5, 10, 20$ respectively, overplotted with the median fit (blue solid line) and 1σ spread (red) and 2σ (pink) spread in fits from their corresponding retrievals.

may indicate the presence of life. While the presence of ozone alone is not a definitive sign of life, it can be associated with the detection of other key biosignature gases to argue for biological activity on a planet.

Finally, we note that our retrieved surface pressures are a critical indication of planetary habitability. Typically, a planet is defined as habitable if it can maintain stable surface liquid water. Given ~ 0.3 bar of pressure, liquid water would be stable over a wide range of temperatures, spanning its freezing point at 273 K to its boiling point at that pressure (350 K).

4.1. *Summary and Future Work*

We have developed the first retrieval framework to study reflected light data from terrestrial planets. Our forward model assumes a cloud-free atmosphere and features Rayleigh scattering due to N_2 as well as absorption due to H_2O and O_3. We implement the `emcee` MCMC sampling suite to construct our posterior distributions. Anticipating the launch of NASA's WFIRST mission, which may be paired with an external starshade, we examine our ability to detect H_2O, O_3, and surface pressure as a function of spectral resolution ($R = 35, 70, 140$) and signal-to-noise ratio (SNR $= 5, 10, 20$). Simulated observations for these studies come from a well-tested 3D spectral model of

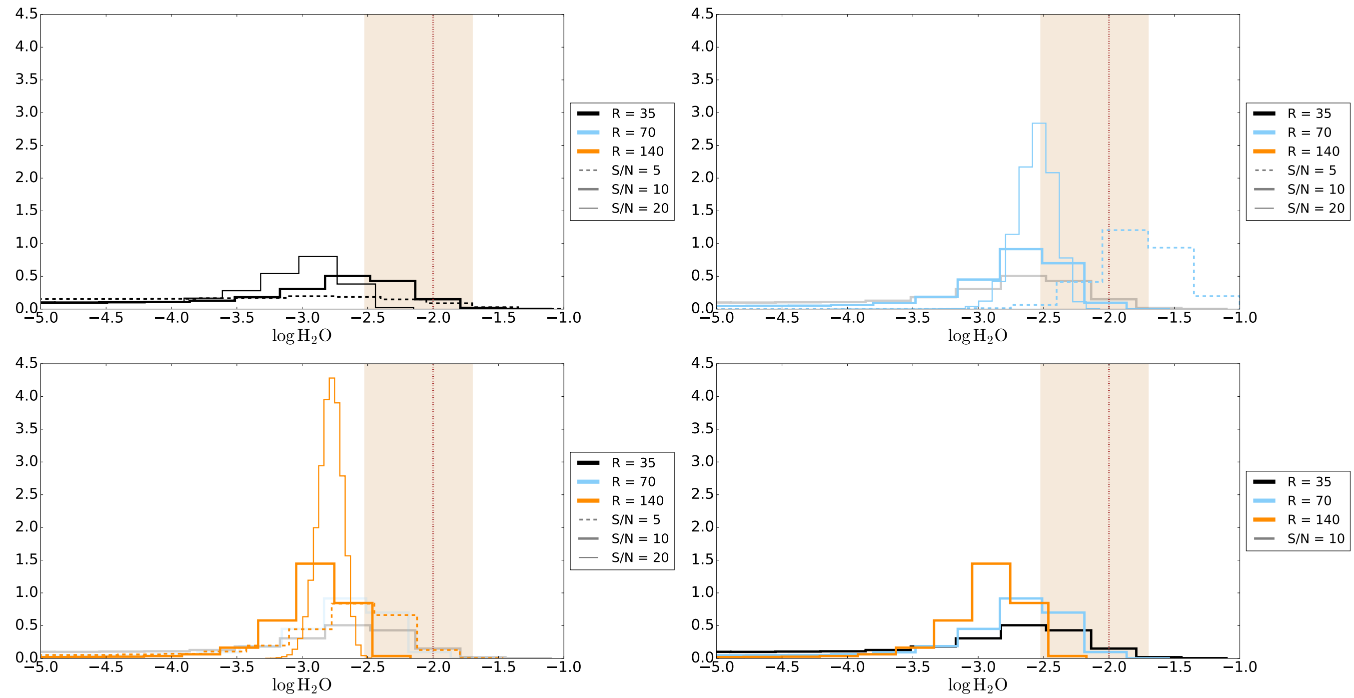

Figure 6. Posterior distributions for H_2O overplotted with the expected model range. There is a bias in the distributions to lower mixing ratios. *Top, left:* $R = 35$ at SNR $= 5, 10, 20$. *Top, right:* $R = 70$ at SNR $= 5, 10, 20$ with $R = 35$, SNR $= 10$ for comparison. *Bottom, left:* $R = 140$ at SNR $= 5, 10, 20$ with both $R = 35$ and $R = 70$ at SNR $= 10$ for comparison. *Bottom, right:* All three R at SNR $= 10$.

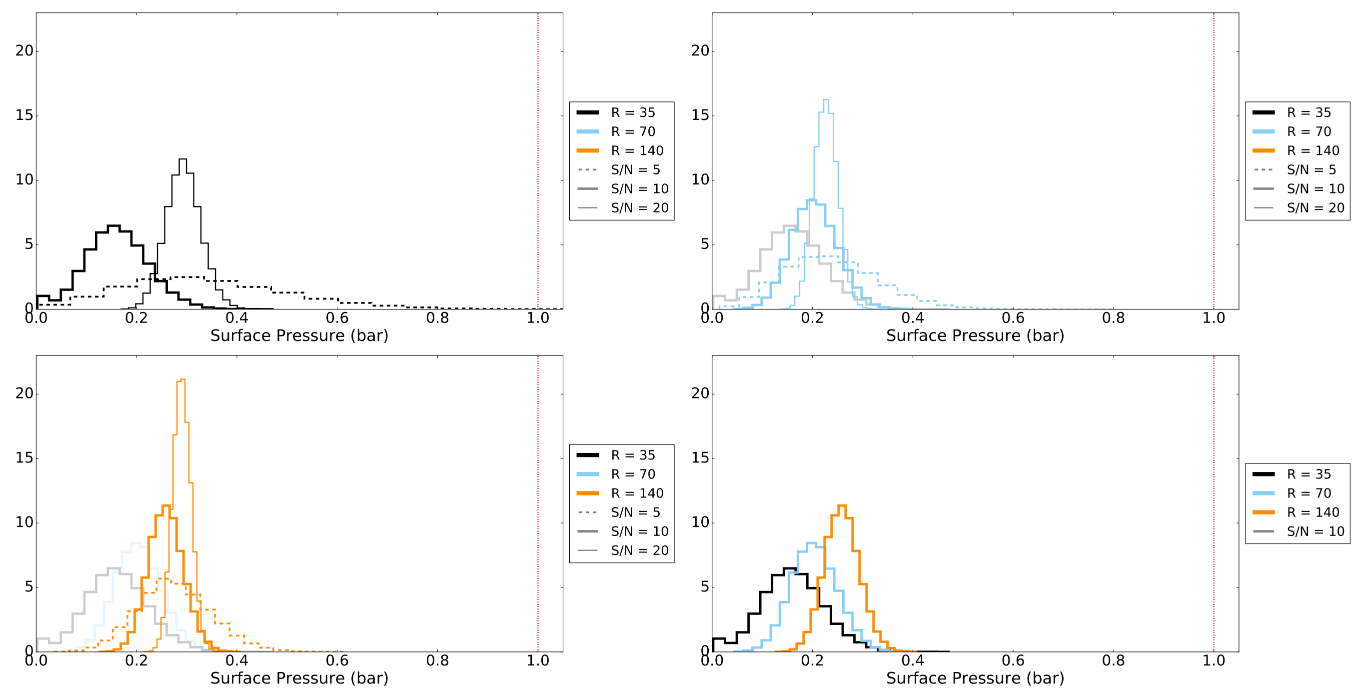

Figure 7. Posterior distributions for surface pressure overplotted with $P = 1$ bar. There is a bias in the distributions to lower surface pressure. *Top, left:* $R = 35$ at SNR $= 5, 10, 20$. *Top, right:* $R = 70$ at SNR $= 5, 10, 20$ with $R = 35$, SNR $= 10$ for comparison. *Bottom, left:* $R = 140$ at SNR $= 5, 10, 20$ with both $R = 35$ and $R = 70$ at SNR $= 10$ for comparison. *Bottom, right:* All three R at SNR $= 10$.

Earth's reflected-light spectrum, which is paired with a WFIRST instrument model that spans 0.4 μm to 1.0 μm in wavelength. We successfully detect all three quantities across the resolutions and signal-to-noise ratios, although our cloud-free assumption biases the H_2O and surface pressure distributions to lower values. The retrieved O_3 mixing

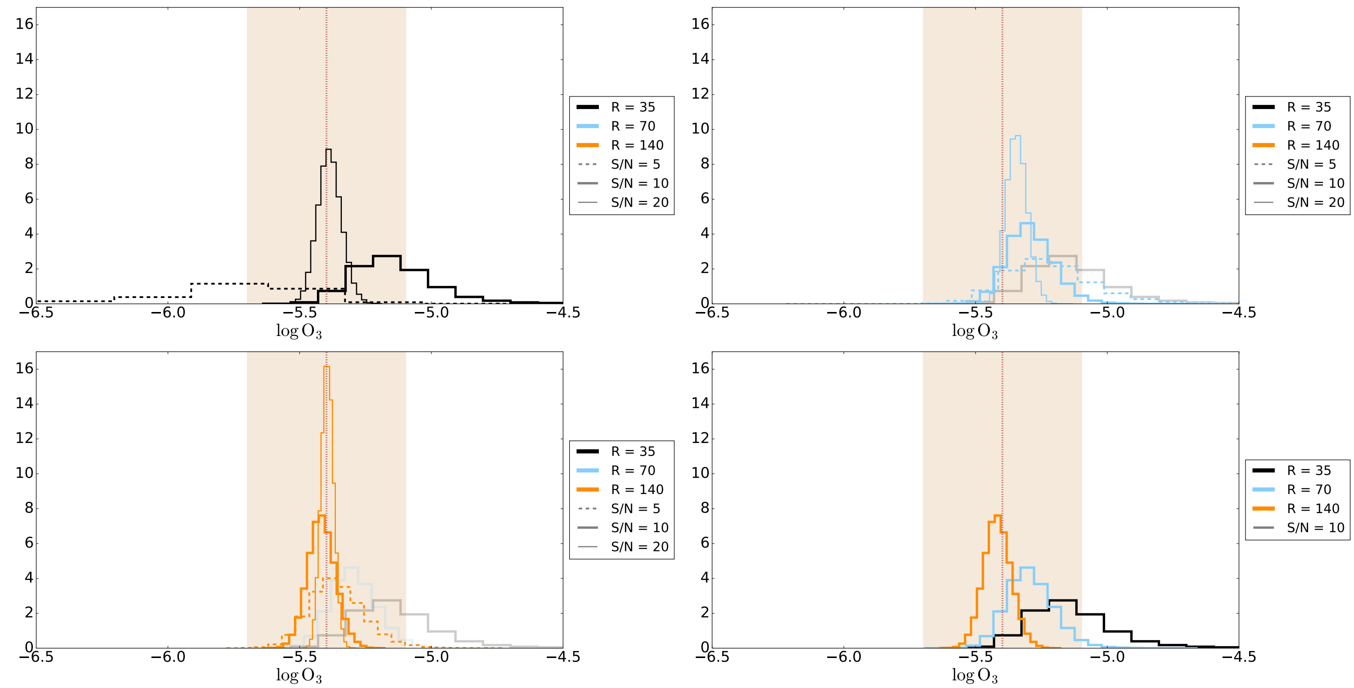

Figure 8. Posterior distributions for O_3 overplotted with the expected model range. Most distributions converge within the expected range. *Top, left:* $R = 35$ at SNR $= 5, 10, 20$. *Top, right:* $R = 70$ at SNR $= 5, 10, 20$ with $R = 35$, SNR $= 10$ for comparison. *Bottom, left:* $R = 140$ at SNR $= 5, 10, 20$ with both $R = 35$ and $R = 70$ at SNR $= 10$ for comparison. *Bottom, right:* All three R at SNR $= 10$.

ratio matches with what is expected of Earth's atmosphere.

Moving forward, we plan to implement a multimodal nested sampling algorithm, `MultiNest`, which is computationally quicker than `emcee`. This improvement in efficiency is advantageous as we look to expanding the forward model. Our current investigation's goal was to determine the simplest physics needed to adequately characterize an Earth-like atmosphere. We have found that the cloud-free assumption hinders our interpretation, especially for the valuable parameters of water vapor mixing ratio and surface pressure, which are both tied to the habitability of a planet. To mitigate this bias, our next forward model will include a parameterization for clouds. In addition, we will include more molecular species, such as O_2. We also plan to expand our studies to other types of small worlds, such as super-Earths and mini-Neptunes. We aim to determine the degree to which we are able to distinguish among the diverse types of atmospheres expected for terrestrials and sub-Neptunes. We will also examine the impact of changing the considered wavelength range. For instance, the drop-off at 0.35 μm in Figure 5 is indicative of an impressive ultraviolet feature for O_3. Allowing flexibility in our wavelength range will aid the development of potential missions such as the Habitable Exoplanet Explorer (HabEx) or Large UV/Optical/Near-IR (LUVOIR) telescope.

We thank the Kavli Foundation for supporting this summer program and providing this opportunity. This work is made possible with support from the National Science Foundation, the Other Worlds Laboratory at UCSC, and the University of California, Santa Cruz. This material is based upon work supported by the National Science Foundation Graduate Research Fellowship under Grant DGE1339067. The computation for this research was performed by the UCSC Hyades supercomputer, which is supported by National Science Foundation (award number AST-1229745) and University of California, Santa Cruz. We thank Mike Line, Roxana Lupu, Mark Marley, Cecilia Leung for stimulating discussions and essential guidance. We thank Jonathan Fortney, the Scientific Organizing Committee, Pascale Garaud, the Local Organizing Committee, and all participants of this summer program for creating a unforgettable educational experience.

REFERENCES

Anglada-Escudé, G., Amado, P. J., Barnes, J., et al. 2016, Nature, 536, 437

Barman, T. S., Macintosh, B., Konopacky, Q. M., & Marois, C. 2011, ApJ, 733, 65

Borucki, W. J., Koch, D. G., Lissauer, J. J., et al. 2003, in Proc. SPIE, Vol. 4854, Future EUV/UV and Visible Space Astrophysics Missions and Instrumentation., ed. J. C. Blades & O. H. W. Siegmund, 129–140

Borucki, W. J., Koch, D. G., Basri, G., et al. 2011, ApJ, 728, 117

Burke, C. J., Christiansen, J. L., Mullally, F., et al. 2015, The Astrophysical Journal, 809, 8

Burrows, A. 2014, ArXiv e-prints, arXiv:1412.6097

Cahoy, K. L., Marley, M. S., & Fortney, J. J. 2010, ApJ, 724, 189

Charbonneau, D., Brown, T. M., Noyes, R. W., & Gilliland, R. L. 2002, ApJ, 568, 377

Cox, A. N. 2000, Allen's astrophysical quantities

de Wit, J., Wakeford, H. R., Gillon, M., et al. 2016, Nature, advance online publication,

Ellingson, R. G., & Fouquart, Y. 1991, Journal of Geophysical Research: Atmospheres, 96, 8925

Feroz, F., & Hobson, M. P. 2008, MNRAS, 384, 449

Feroz, F., Hobson, M. P., & Bridges, M. 2009, MNRAS, 398, 1601

Foreman-Mackey, D., Hogg, D. W., Lang, D., & Goodman, J. 2013, PASP, 125, 306

Goodman, J., & Weare, J. 2010, Commun. Appl. Math. Comput. Sci., 5, 65

Greco, J. P., & Burrows, A. 2015, ApJ, 808, 172

Hansen, J. E., & Travis, L. D. 1974, SSRv, 16, 527

Horak, H. G. 1950, ApJ, 112, 445

Horak, H. G., & Little, S. J. 1965, ApJS, 11, 373

Lupu, R. E., Marley, M. S., Lewis, N., et al. 2016, ArXiv e-prints, arXiv:1604.05370

Macintosh, B., Graham, J. R., Barman, T., et al. 2015, Science, 350, 64

Marley, M., Lupu, R., Lewis, N., et al. 2014, ArXiv e-prints, arXiv:1412.8440

Marley, M. S., Gelino, C., Stephens, D., Lunine, J. I., & Freedman, R. 1999, ApJ, 513, 879

Mayor, M., & Queloz, D. 1995, Nature, 378, 355

McClatchey, R. A., Fenn, R. W., Selby, J. E. A., Volz, F. E., & Garing, J. S. 1972, Optical Properties of the Atmosphere 3rd edn

McKay, C. P., Pollack, J. B., & Courtin, R. 1989, Icarus, 80, 23

Meadows, V. S., & Crisp, D. 1996, J. Geophys. Res., 101, 4595

Pallé, E., Goode, P. R., Montañés-Rodríguez, P., & Koonin, S. E. 2004, Science, 304, 1299

Robinson, T. D., Stapelfeldt, K. R., & Marley, M. S. 2016, PASP, 128, 025003

Robinson, T. D., Meadows, V. S., Crisp, D., et al. 2011, Astrobiology, 11, 393

Spergel, D., Gehrels, N., Breckinridge, J., et al. 2013, ArXiv e-prints, arXiv:1305.5422

Spergel, D., Gehrels, N., Baltay, C., et al. 2015, ArXiv e-prints, arXiv:1503.03757

Toon, O. B., McKay, C. P., Ackerman, T. P., & Santhanam, K. 1989, Journal of Geophysical Research, 94, 16287

Traub, W. A., Breckinridge, J., Greene, T. P., et al. 2016, Journal of Astronomical Telescopes, Instruments, and Systems, 2, 011020

Turnbull, M. C., Glassman, T., Roberge, A., et al. 2012, PASP, 124, 418